Single-Nanoparticle Near-Infrared Surface Plasmon Resonance Microscopy for Real-Time Measurements of DNA Hybridization Adsorption

Aaron R. Halpern, Jennifer B. Wood, Yong Wang, and Robert M. Corn*

Department of Chemistry, University of California—Irvine, Irvine, California 92697, United States

ABSTRACT A novel 814 nm near-infrared surface plasmon resonance (SPR) microscope is used for the real-time detection of the sequence-selective hybridization adsorption of single DNA-functionalized gold nanoparticles. The objective-coupled, high numerical aperture SPR microscope is capable of imaging *in situ* the adsorption of single polystyrene and gold particles with diameters ranging from 450 to 20 nm onto a 90 μm $\times$ 70 μm area of a gold thin film with a time resolution of approximately 1−3 s. Initial real-time SPR imaging (SPRI) measurements were performed to detect the accumulation of 40 nm gold nanoparticles for 10 min onto a gold thin film functionalized with a 100% complementary DNA surface at concentrations from 5 pM to 100 fM by counting individual particle binding events. A 100% noncomplementary DNA surface exhibited virtually no nanoparticle adsorption. In contrast, in a second set of SPRI measurements, two component complementary/noncomplementary mixed DNA monolayers that contained a very small percentage of complementary sequences ranging from 0.1 to 0.001%, showed both permanent and transient hybridization adsorption of the gold nanoparticles that could be tracked both temporally and spatially with the SPR microscope. These experiments demonstrate that SPR imaging measurements of single biofunctionalized nanoparticles can be incorporated into bioaffinity biosensing methods at subpicomolar concentrations.

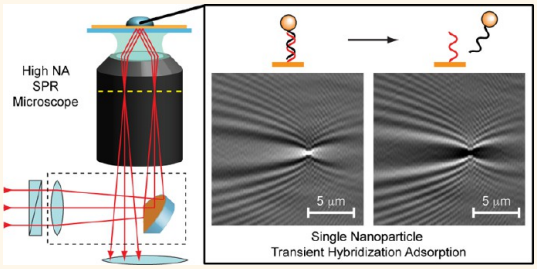

KEYWORDS: surface plasmon resonance imaging · surface plasmon resonance microscopy · DNA hybridization adsorption · gold nanoparticles · polystyrene nanoparticles

Surface plasmon resonance (SPR) techniques are ideally suited to measure surface bioaffinity adsorption by taking advantage of the sensitivity of the interfacial surface plasmon polaritons (SPPs) to the local refractive index (RI) of the dielectric.[1] To overcome the lack of biomolecule selectivity of RI sensing, multiplexed measurements using array-based SPR imaging (SPRI) have been favored to detect the specific interactions between biologically relevant species such as DNA, RNA, and proteins.[2−4] Although a variety of methods exist for increasing the sensitivity of SPRI, perhaps the most successful and widespread approach is the technique of nanoparticle-enhanced SPR.[5] Nanoparticles with a range of sizes, shapes, and materials have been applied in a variety of SPRI sensor configurations for the enhanced detection of metal ions, small molecules, nucleic acids, and proteins.[6−10] In the general case for DNA sensing, Au nanoparticles are functionalized with thiolated oligonucleotides,[11] and upon hybridization adsorption to a complementary surface sequence, the resulting RI change caused by the gold colloid can grant a 1000-fold increase in SPR signal.[12] Furthermore, it is possible to couple enzymatic amplification with nanoparticle-enhanced SPR for even greater sensitivity.[13]

SPRI measurements are usually conducted on the macroscopic scale by simultaneously monitoring tens to hundreds of individual sensor elements that can range from 0.01 to 1 mm^2 in area.[14] In recent years, there has been increased interest in the use of microscope objectives for high-resolution SPRI measurements of surface interactions on the microscale. For example,

* Address correspondence to rcorn@uci.edu.

Received for review November 12, 2013 and accepted December 18, 2013.

Published online December 18, 2013
10.1021/nn405868e

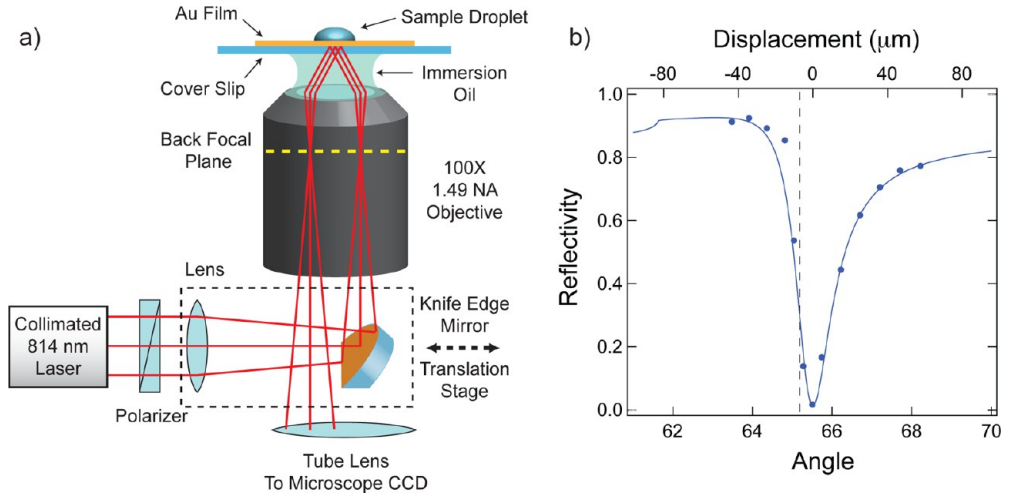

Figure 1. (a) Schematic diagram of the NIR, objective-coupled, high NA SPR microscope utilizing a knife-edge mirror. (b) *In situ* SPR curve of a gold-coated coverslip at 814 nm sampled on the SPR microscope (dots) with a four-phase Fresnel calculation fit for a BK7/Cr/Au/H_2O interface (solid).

SPR microscopes have been used to study proteins binding to micropatterns,[15] cell–substrate interactions,[16–24] or image individual nanoparticles[25–28] and their catalytic activity.[29]

For the construction of an SPR microscope, a variety of coupling methods are available. The simplest method involves a prism coupling and an objective lens for imaging; however, this geometry suffers from long working distances and image distortions.[26–28,30] Alternatively, solely a high numerical aperture (NA), oil immersion objective can provide the coupling to a gold-coated coverslip. Light focused by the high NA objective can be used to locally excite SPPs,[31] but the image must be raster scanned and reconstructed by Fourier plane analysis[32,33] or by interferometry.[34,35] On the other hand, the high NA objective can be used to output collimated light at high incidence angles and simultaneously collect the reflected image. This is achieved by focusing input light onto the back focal plane (BFP) of the objective with an offset from the center to set the incidence angle.[36]

In this work, we will combine a high NA SPR microscope with the technique of nanoparticle-enhanced SPRI to image single-nanoparticle DNA hybridization adsorption events in real-time. First, a near-infrared (NIR) SPR microscope is described with two key innovations: (1) an 814 nm wavelength was selected to provide a smaller SPR angle and greater SPR sensitivity as compared to visible wavelengths used in the microscopes noted previously, and (2) a knife-edge mirror was used to redirect the focused input light, yet allow the reflected image to be collected by the microscope tube lens to eliminate fringing caused by multiple reflections. The microscope was characterized with dielectric polystyrene (PS) nanoparticles from 450 to 85 nm in diameter and metallic Au nanoparticles from 100 to 20 nm in diameter. Next, single-particle hybridization adsorption events of DNA-modified 40 nm Au nanoparticles onto 100% complementary surfaces were counted at concentrations from 5 pM to 100 fM. Finally, two component mixed DNA monolayers that contained a very small percentage of complementary sequences ranging from 0.1 to 0.001% were used to detect permanent and transient single-particle adsorption events.

RESULTS AND DISCUSSION

NIR SPR Microscope Construction and Characterization. The SPR microscope relies on a high numerical aperture, oil immersion objective, capable of focusing light at high incidence angles to achieve the excitation of SPPs on a gold-coated coverslip. The optical setup, shown schematically in Figure 1a, is based on the work of Huang *et al.* with two key modifications.[36] The first modification was the selection of an 814 nm NIR diode laser source for two reasons: (1) it is in the wavelength range determined for maximum SPR sensitivity, as compared to shorter visible wavelengths,[37,38] and (2) it narrows and shifts the SPR angle, θ_{spr}, to lower incidence angles.[39] This has an important consequence for selecting an immersion objective when constructing an SPR microscope. For example, at 814 nm, $\theta_{spr} = \sim 65.5°$, whereas at 633 nm, $\theta_{spr} = \sim 75.7°$. Although we have used a 1.49 NA objective in this work, selecting 814 nm (or longer wavelengths) will offer the advantage of allowing for more common, less expensive 1.4 NA objectives that can only attain a maximum half angle of 67.5°, still large enough for SPR imaging on the steep half of the SPR curve.

The NIR laser light was prepared for the SPR microscope by passing it through a spatial filter to expand and collimate the beam. The polarization and intensity was controlled by a $\lambda/2$ plate (not shown) and a linear polarizer placed before and after the spatial filter,

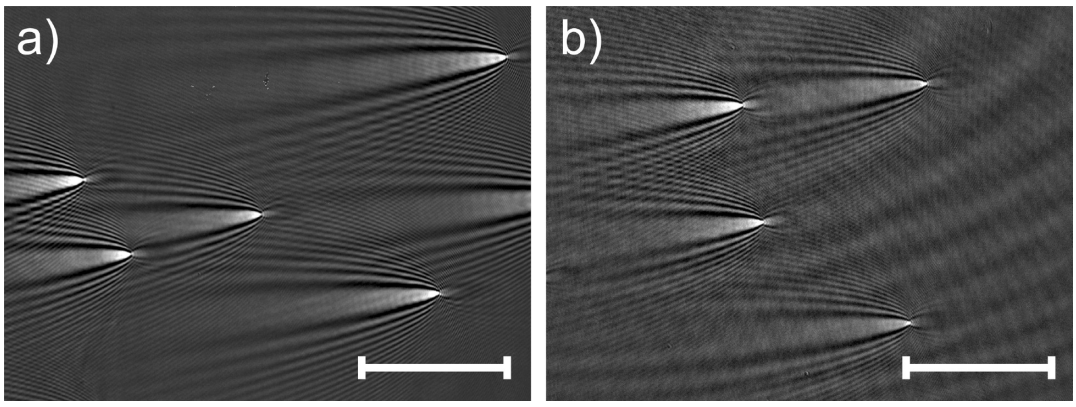

Figure 2. SPR microscope difference images of (a) 200 nm polystyrene and (b) 50 nm Au nanoparticles. Scale bars are 25 μm.

respectively. For macroscopic SPR imaging, it is important to illuminate the sample with a highly collimated beam to limit the broadening of the SPR resonance curve. In the case of the SPR microscope, in order to output collimated light from the front element of the objective, a lens was used to focus the input light onto the back focal plane of the objective.[36] The second modification was the implementation of a gold-coated knife-edge mirror to direct the focused light upward into the objective. The mirror is positioned so it can redirect the focused input beam yet allows the reflected image collected by the objective to pass without being clipped. Typically, objective-coupled SPR microscopes use a beam splitter to redirect the focused light and simultaneously collect the reflected image;[25,36] however, the mirror offers two advantages over beam splitting optics: (1) the mirror enables the collection of the full amplitude of the signal since no light is lost to splitting, and (2) interference effects that might occur from multiple reflections are eliminated.

To tune the incidence angle on the sample, the lens and mirror are coupled together on a linear translation stage and translated across the center axis of the objective. The *in situ* reflectivity curve shown in Figure 1b was collected by translating the mirror in 10 and 5 μm increments across the SPR resonance. The full SPR curve was obtained by translating the mirror by only 100 μm, with the steepest half of the SPR curve occurring in only ~20 μm of displacement. A theoretical curve was fit as a function of incidence angle using a four-phase Fresnel calculation for a BK7/Cr/Au/H_2O interface using the minimum of the SPR curve as a reference point (displacement = 0).

To image *in situ* adsorption of individual nanoparticles, the incidence angle was set to 30% reflectivity on the SPR curve, as denoted by the vertical dotted line in Figure 1b. The gold surface was previously modified with a positively charged monolayer of 11-mercaptoundecamine (MUAM) and was protected by a small droplet of water contained in a silicone isolation well. A solution of either negatively charged polystyrene or Au nanoparticles was then spiked into the droplet, and electrostatic adsorption was monitored by continuously taking the difference image between the most recently acquired frame and the previously acquired frame. Note that a nanoparticle will only appear in the difference image when it initially adsorbs onto the surface since the nanoparticle causes an instantaneous localized increase of reflectivity; in subsequent difference images, if both frames contain the nanoparticle, then no difference will appear. This frame-by-frame difference imaging eliminates any long-term intensity fluctuations caused by the light source or by the focus drift.

Example difference images of PS or Au particles are shown in Figure 2. Five 200 nm diameter PS particles can be seen in the difference image at the moment they bind to the surface in Figure 2a. The nanoparticle response pattern appears as a bright center region with alternating positive and negative tails flowing to the left—in the direction of plasmon propagation. For these particles, the tails are visible for up to 50 μm and are due to the long surface plasmon propagation length in the NIR. Also visible are the interference patterns that result when the tails of nearby nanoparticles overlap. Considerably shorter tails have been previously observed in SPR images of nanoparticles in works using visible wavelengths.[25,27]

To determine if there is a material dependence on the response pattern, the adsorption of Au nanoparticles was also observed. The response pattern for 50 nm diameter Au particles is identical to that of PS, as seen in the image in Figure 2b. The slight differences in the PS and Au images are the result of inaccuracies in setting the microscope focus before the image acquisition. We believe that the tails that appear to the right of the bright center region (in the direction opposite to the plasmon propagation) are also attributed to the microscope being slightly out of focus, due to the shallow depth of the field of the objective.

A variety of particle sizes, from 450 to 85 nm diameter PS particles and from 100 to 20 nm diameter Au particles, were observed in this manner using the SPR microscope. The change in reflectivity ($\Delta\%R$)

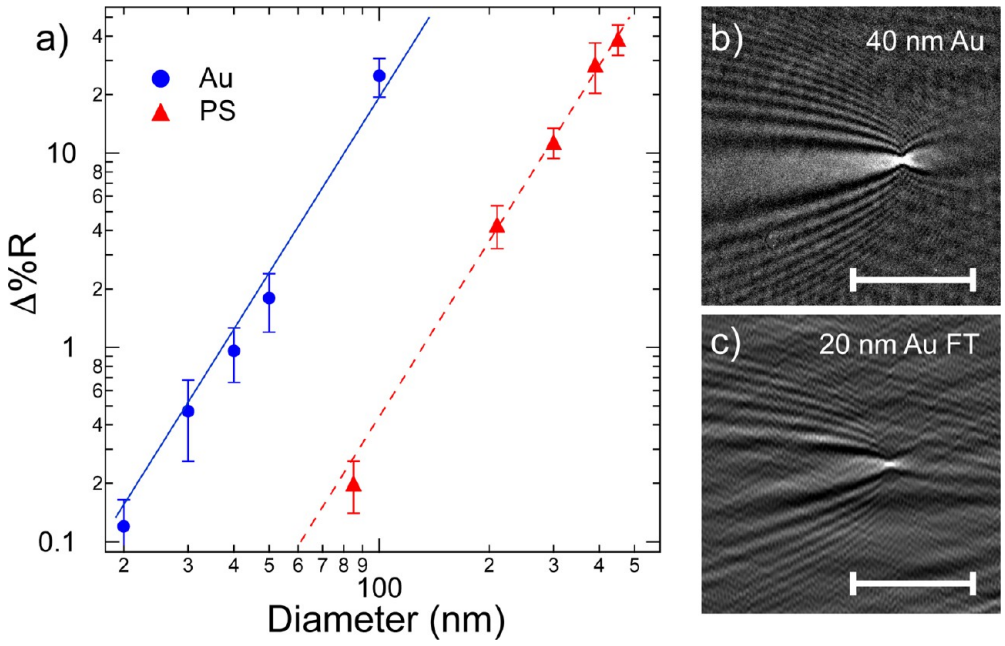

Figure 3. (a) Change in reflectivity, Δ%*R*, of a variety of sizes of Au (blue dots) and PS (red triangles) particles fit to functions of the diameter cubed. (b) Difference image of a 40 nm Au nanoparticle and (c) Fourier filtered difference image of a 20 nm Au nanoparticle. Scale bars are 10 μm.

values of Au (blue circles) and PS (red triangles) as a function of particle diameter are displayed on a log−log plot as shown in Figure 3a. The Δ%*R* value for each particle was calculated by dividing the peak intensity of the difference image by the intensity of the raw frame and multiplying by 0.3 (the angle was set at approximately 30% reflectivity). For the PS particles, the largest particles (450 nm) caused a massive increase of ~40 Δ%*R*, while the 200 nm particles displayed in Figure 2a showed only ~4 Δ%*R*. The smallest PS particle imaged was 85 nm and displayed ~0.2 Δ%*R*. For Au particles, the largest particles (100 nm) caused an increase of ~20 Δ%*R*, while the 50 nm particles displayed in Figure 2b caused an increase of ~2 Δ%*R*. For DNA hybridization adsorption experiments, we have decided to use the 40 nm Au particles such as the one displayed in the SPR difference image in Figure 3b. These particles were easy to detect (~1 Δ%*R*), and their signal was not overwhelming, as with larger particles such as the ones shown in Figure 2b. The smallest Au particles that a Δ%*R* value was obtained for were 20 nm in diameter and showed an increase of ~0.1 Δ%*R*. To make the response of the small particle more apparent, a custom Fourier filter was used, resulting in the image displayed in Figure 3c. This Fourier filter was used in later sections for easy visualizing of particle binding. The filtering procedure is described in the Supporting Information.

The data in Figure 3a were fit as a function of the diameter cubed and therefore appears on the log scale as a line with a slope of 3. This clearly shows that the magnitude of Δ%*R* is dependent on the volume of the nanoparticle, as has been previously demonstrated experimentally[25,27] and theoretically.[40] For each particle size, the Δ%*R* values for at least 25 particles were averaged. The distribution of Δ%*R* values may be caused by the distribution of the particle sizes in solution, as well as from the assumption that all imaging takes place at the 30% reflectivity point on the SPR curve.

Real-Time Single-Nanoparticle SPRI Measurements of DNA Hybridization Adsorption onto 100% Complementary DNA Monolayers. In order to observe single-nanoparticle binding events caused by DNA hybridization adsorption, 40 nm Au particles were modified with thiolated T_{30} oligonucleotides following the procedure detailed by Hurst *et al.*[11] A solution containing 1 pM of these particles was exposed to a gold surface modified with a full monolayer of A_{30} thiolated oligonucleotide, and the hybridization adsorption was observed with the SPR microscope. Figure 4a is a 90 × 70 μm^2 Fourier filtered difference image showing the binding of five nanoparticles marked by the red circles. Overlaid on this image is a particle binding map showing the position of every particle that bound to the surface over the course of the 300 s experiment as marked by the yellow dots. These data can be displayed as a kinetic binding curve; the number of particles bound in each difference image was counted and added cumulatively as shown in Figure 4b. The particles were injected after 30 s, and over the course of 300 s, a total of 152 particles bound to the surface. We attribute the shape of the binding curve to the diffusion of nanoparticles to the surface since there was no active mixing. As a control, the solution of nanoparticles was exposed to the noncomplementary sequence (SeqA), and only one

particle was observed binding to the surface (blue curve in Figure 4b).

Binding curves for a range of nanoparticle concentrations, from 5 pM to 100 fM, were obtained and displayed on the semilog plot in Figure 5a. Each binding curve has the same shape as the 1 pM data in Figure 4b when plotted in a linear scale. For the highest concentration of nanoparticles (5 pM), over 1000 particles were counted binding to the surface (blue curve). In comparison, for the lowest concentration (100 fM), only 11 particles were counted and the digital nature of the binding events is apparent from the black curve in Figure 5a. As expected, the total number of particles counted for each concentration of nanoparticles followed a linear relationship as shown in Figure 5b. Error bars are assigned as a percentage of the total signal since particles cannot be counted in the few frames following the initial injection of the nanoparticle solution from the large disturbance it caused before the difference images stabilized. Each concentration of particles was also run on a noncomplementary surface that displayed negligible nonspecific binding (3 counts for the 5 pM, 1 count for 1 pM, and zero for concentrations below). We note that, due to the surface docking area of each 40 nm nanoparticle, it is highly likely that each binding event is the result of hybridization between multiple DNA strands on the nanoparticle and the surface. We will deal with the case of a nanoparticle binding to a single surface strand by creating mixed surface monolayers of complementary and noncomplementary DNA in the following section.

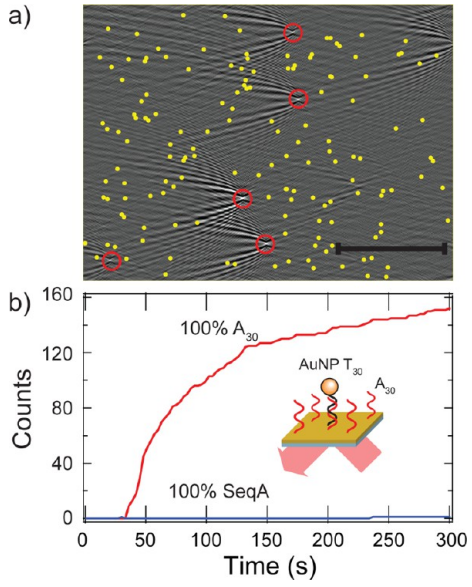

Figure 4. (a) Fourier filtered difference image of a 1 pM solution of T_{30} nanoparticles binding to a complementary surface showing five binding events (red circles). The locations of all the particles bound after 300 s are marked by yellow dots and are overlaid on the image. Scale bar is 25 μm. (b) Particle binding curves for the 1 pM solution onto complementary (red) and noncomplementary (blue) surfaces over the 300 s.

Real-Time Single-Nanoparticle SPRI Measurements of DNA Hybridization Adsorption onto Two Sequence Complementary/Noncomplementary Mixed DNA Monolayers. As an alternative to detecting low concentrations of particles in solution, the SPR microscope was tested to detect low surface coverages of a complementary sequence. As a model system, mixed monolayers consisting of 0.1 to 0.001% of the complementary sequence (A_{30}), diluted by a noncomplementary sequence (SeqA), were formed on gold coverslips.[41] The surfaces were then exposed to a 30 pM solution of the T_{30}-modified nanoparticles. In these experiments, only a small fraction of the surface sites were available for hybridization. Using literature values for a fully packed monolayer of $\sim 7 \times 10^{12}$ DNA molecules/cm^2, on average, there will be only one complementary sequence in a 40 $\times$ 40 nm^2 area for a 0.1% monolayer.[42] We therefore assume for the experiments with the mixed monolayers that each particle that bound to the surface was the result of a single DNA–DNA hybridization.

The usage of the two sequence mixed monolayers had an unforeseen effect on the nanoparticle binding behavior. For this example using a mixed monolayer of 0.01% A_{30}, we observed nanoparticle binding events such as the image shown in Figure 6a. As seen previously, this is indicative of a particle binding to the surface, and we deem this as a "positive" binding event,

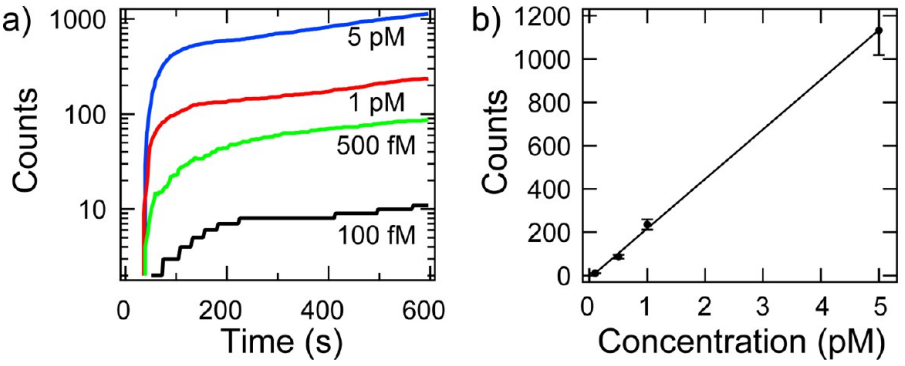

Figure 5. (a) Particle binding curves as a function of time for nanoparticle solutions from 5 to 0.1 pM and (b) total particle counts as a function of concentration after 10 min.

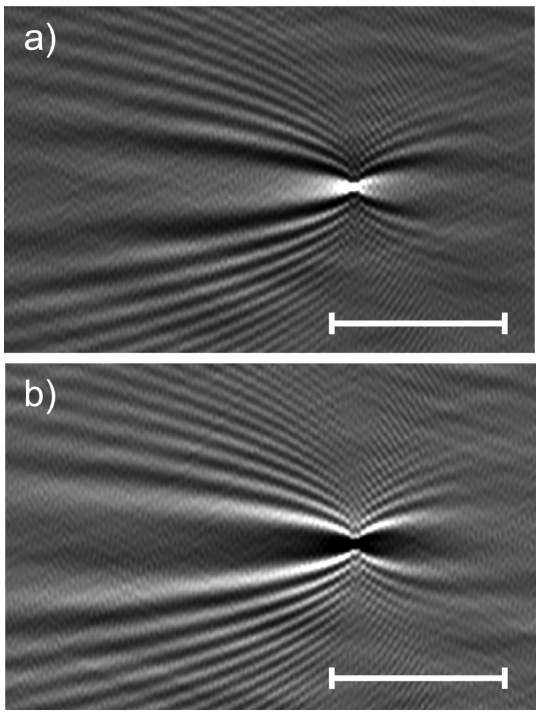

Figure 6. Transient adsorption of a T_{30} 40 nm Au onto a mixed monolayer containing 0.01% A_{30}. (a) Difference image of a nanoparticle adsorption denoted as a "positive" particle binding event and (b) its subsequent desorption denoted as a "negative" particle binding event. Scale bars are 10 μm.

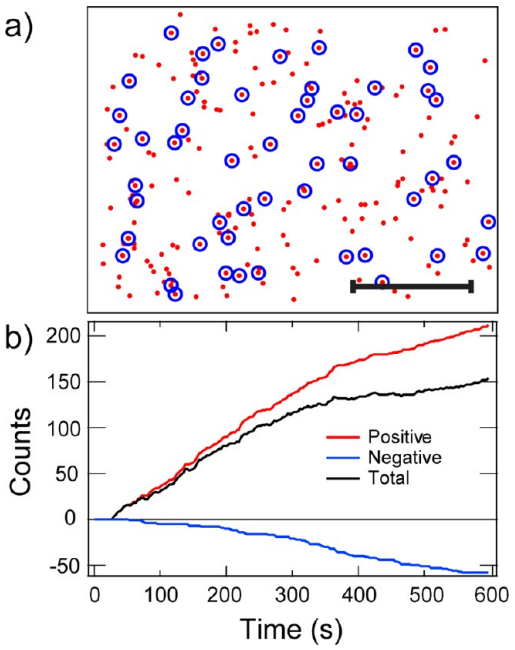

Figure 7. (a) Binding map of T_{30} 40 nm Au nanoparticle positive adsorption (red dots) and negative desorption (blue circles) onto a mixed monolayer containing 0.01% A_{30}. Scale bar is 25 μm. (b) Positive (red) and negative (blue) counts as a function of time. The black curve is the sum of the two and represents permanently adsorbed particles.

in accordance with positive reflectivity change at the bright center region. However, in the exact same location in the following difference image shown in Figure 6b, an inverse intensity pattern compared to Figure 6a was observed, with a negative difference in the dark center region. This can only be due to the particle leaving the surface, causing a decrease in reflectivity; we deem this a "negative" event. We attribute this behavior to transient adsorption of nanoparticles to the surface; a particle adsorbs to the surface causing a positive event followed shortly by desorption causing a negative event. In the example shown in Figure 6a,b, the particle was released from the surface after just one frame (3 s). Typically, the particles were transiently adsorbed for a few frames; however, we have observed particles having transient adsorptions lasting up to 15 frames. This transient adsorption behavior was observed for all the mixed monolayer surfaces.

For the 0.01% A_{30} surface, a particle binding map was generated with the locations of all the positive (red dot) and negative (blue circle) binding events as shown in Figure 7a. Evident from the map, no particle desorption exists without a prior adsorption, as should be expected. The accumulation of positive and negative binding events over time is plotted in Figure 7b, with the black binding curve showing the amount of particles permanently adsorbed. For this surface, approximately 25% of the events were transient adsorptions, with ~200 positive events and ~50 negative events. For comparison, when the same nanoparticles were exposed to a full noncomplementary surface (100% SeqA and 0% A_{30}), there were only 17 positive events and 13 negative events, with a net of only 4 particles nonspecifically adsorbed. Since the amount of positive and negative events depends on the percentage of A_{30} on the surface, we believe that the transient adsorption was due to weakly bound nanoparticles held by only a few A–T base pairs.

Binding curves from mixed monolayer with 0.1 to 0.001% A_{30} are compiled in the semilog plot as shown in Figure 8a. For the 0.1% surface coverage, over 1000 permanent binding events were observed, whereas for 0.001%, only 11 permanent events were counted. Again, the digital nature of particle binding can be seen in the lower surface coverages; however, this time, positive and negative fluctuations can be seen as a result of particle transient adsorptions. These data can be plotted as a function of the percent of A_{30} in the mixed monolayer as displayed in Figure 8b and fit to a linear relationship as expected. The error bars are assigned as a percent of the total counts for the same reason as Figure 5b.

For comparison of the detection limits of these two types of experiments, the 100% complementary monolayer and the low percentage mixed monolayers, we refer to the Langmuir isotherm. At low concentration, we assume $\theta \approx CK_{ads}$, where θ is the equilibrium surface coverage, C is the concentration, and K_{ads} is

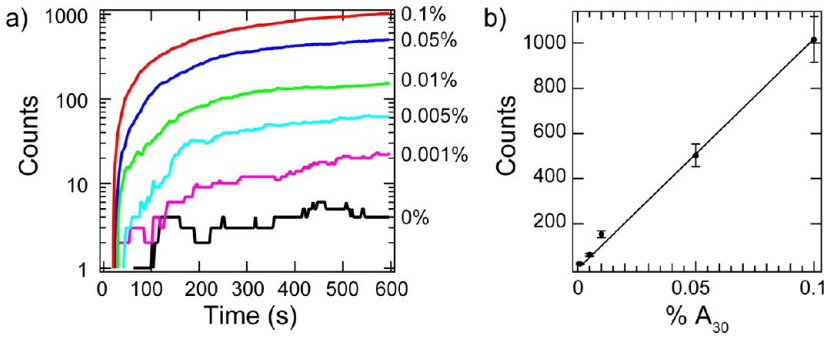

Figure 8. (a) Binding curves of permanently adsorbed T_{30} 40 nm Au nanoparticles onto mixed monolayers containing 0.1 to 0.001% A_{30} and (b) total particle counts as a function of %A_{30}.

the Langmuir adsorption coefficient. Using a K_{ads} = 1.8×10^7 M^{-1} for DNA hybridization[3] and a minimum detected surface coverage of θ = 0.001% corresponds to a concentration detection limit of 50 fM, similar to the 100 fM of nanoparticles detected on the 100% complementary surface.

CONCLUSIONS

In this paper, we have described a NIR, objective-coupled, high numerical aperture SPR microscope. Two key modifications enabled the real-time imaging of single-nanoparticle binding events caused by DNA hybridization adsorption. First, the usage of an 814 nm wavelength decreased the SPR angle and increased the SPR sensitivity compared to visible wavelengths. Although the longer propagation length of the NIR wavelength causes a decrease in spatial resolution in the direction of plasmon propagation, we were able to localize single nanoparticles by their unique response pattern. Second, a knife-edge mirror was used in place of a beam splitter to collect the full SPR signal and eliminate interference patterns. DNA-modified 40 nm Au nanoparticles with concentrations from 5 to 0.1 pM were detected on a full monolayer of a complementary sequence by counting individual nanoparticle binding events. We expect that single-nanoparticle SPRI should be directly applicable to study other nanoparticle-enhanced assays at low concentrations such as miRNA capture and detection.[8] An alternative to detecting low nanoparticle concentrations in solution was performed by creating two sequence mixed monolayers composed of 0.1 to 0.001% of complementary DNA. At these low surface coverages, both permanent nanoparticle adsorption caused by single DNA−DNA hybridization and transient adsorption were observed. This transient adsorption behavior is reported for the first time using SPRM and was assigned to be weakly bound particles caused by a few A−T base pairs; however, additional experiments on sequence dependence and particle dwell time are needed to fully understand this behavior. In comparison with the surface-sensitive microscopy techinques of single-molecule total internal reflection fluorescence (TIRF), SPRM offers the advantage of being able to continuously monitor individual binding events without the need to account for photobleaching or blinking of the fluorophores.[43] In the future, we anticipate the combination of nanoparticle detection with enzymatic amplification to study complex systems such as the polyadenylation reaction of single poly(A) polymerases[13] or the formation of microscopic DNA surface clusters.[44]

METHODS

Optical Setup. The SPR microscope was built in the configuration as shown in Figure 1a using the frame of an IX51 inverted microscope (Olympus, Tokyo, Japan). A 1 mW 814 nm diode laser (Melles Griot, Carlsbad, CA) was expanded and collimated using a spatial filter (Newport Corp., Newport Beach, CA). The beam was polarized and focused with a lens (f = 200 mm) onto the back focal plane of a 100× 1.49 NA oil objective (Olympus). The focused beam was directed upward near the edge of the objective by a gold-coated knife-edge D-shaped mirror (Thorlabs, Newton, NJ) while allowing the reflected image to pass out the other side. The focusing lens and D mirror were mounted on an $X-Y$ micrometer to adjust the incident angle on the sample. Images were acquired on an Andor Neo sCMOS (South Windsor, CT) by accumulating 30 11-bit exposures. This setup is similar to the one described by Huang *et al.*[36] Samples were borosilicate No. 1.5 coverslips (Fisherbrand, Pittsburgh, PA) coated with a 1 nm adhesion layer of chromium, followed by 45 nm of gold using a thermal evaporator.

Polystyrene and Gold Nanoparticle Size Analysis. Carboxyl-coated polystyrene beads were purchased from Invitrogen (Carlsbad, CA) with mean diameters of 0.45, 0.39, 0.30, and 0.21 μm and from Polysciences (Warrington, PA) with a mean diameter of 85 nm. Unmodified gold colloid was purchased from Ted Pella (Redding, CA) in diameters of 100, 50, 40, 30, and 20 nm. Positively charged alkanethiol monolayers (11-mercapto-undecamine, MUAM, Dojindo, Japan) were freshly prepared on the gold-coated coverslips by immersion in a 1 mM solution for 12 h. Adhesive silicone isolation wells (Electron Microscopy Sciences, Hatfield, PA) were used to partition the gold surface and filled with 5 μL of water to protect the MUAM. A 5 μL volume of particle solution (~10^9 particles/mL) was injected into a well, and the electrostatic adsorption of nanoparticles was observed.

DNA Sequences. All DNA was purchased from IDT (Integrated DNA Technologies, Coralville, Iowa) and stored in 1× PBS buffer (11.9 mM phosphates, 137 mM sodium chloride, 2.7 mM

potassium chloride, pH 7.4, Fisher). The DNA sequences were 5′-S-S$(CH_2)_6T_{30}$-3′, 5′-S-S$(CH_2)_6A_{30}$-3′, and a control sequence, 5′-S-S$(CH_2)_6$TTC GGT TCG TGC TTA TGT GTC TGG ATT TCG-3′, which is denoted as SeqA.

DNA Modification of Gold Nanoparticles. Gold nanoparticles (40 nm) were modified following the procedure detailed by Hurst *et al.*[11] Briefly described, 5 μL of 1 mM T_{30} thiolated oligonucleotide was added to 1 mL of ~150 pM nanoparticle stock solution, and the solution was then spiked with aliquots of 2 M NaCl to increase the concentration to 0.01, 0.05, 0.1, and then to 1 M in 0.1 M increments. After each spike, the solution was mixed, sonicated for 10 s, and allowed to rest for 20 min. After reaching the final concentration of NaCl, the solution was allowed to rest overnight. To remove unreacted DNA, the nanoparticles were washed three times by centrifugation at 8000 rcf for 7 min and resuspended in 1× PBS buffer. Throughout the course of the process, the concentration of SDS was kept at 0.01% w/v, except for the final resuspension in PBS. The concentration of particles after washing was determined to be approximately 40 pM by UV−vis absorption.

DNA Surface Modification and Nanoparticle Hybridization Experiments. Gold-coated coverslips were partitioned with silicone isolation wells and exposed to 5 μL of 250 μM thiolated DNA in PBS for 12 h. For full complementary monolayer experiments, the surfaces were modified with 100% A_{30}. For the mixed monolayer experiments, thiol A_{30} and thiol SeqA were diluted to the desired ratio (from 0.1 to 0.001% A_{30}), while keeping the total concentration of DNA constant at 250 μM. The surfaces were rinsed, and 3 μL of buffer was put into each well under a coverslip until the sample was ready to use. To observe the hybridization of the T_{30}-modified gold nanoparticles, 9 μL of particle solution was injected onto the surface and briefly mixed before imaging.

Conflict of Interest: The authors declare no competing financial interest.

Acknowledgment. This work was supported by the NSF through grant CHE-1057638. The authors would like to acknowledge Prof. E. Potma and Prof. E. Botvinick for lending optical components and helpful discussions.

Supporting Information Available: Fourier filtering of nanoparticle SPR difference images. This material is available free of charge *via* the Internet at http://pubs.acs.org.

REFERENCES AND NOTES

1. Homola, J. Surface Plasmon Resonance Sensors for Detection of Chemical and Biological Species. *Chem. Rev.* **2008**, *108*, 462–493.
2. Brockman, J. M.; Nelson, B. P.; Corn, R. M. Surface Plasmon Resonance Imaging Measurements of Ultrathin Organic Films. *Annu. Rev. Phys. Chem.* **2000**, *51*, 41–63.
3. Nelson, B. P.; Grimsrud, T. E.; Liles, M. R.; Goodman, R. M.; Corn, R. M. Surface Plasmon Resonance Imaging Measurements of DNA and RNA Hybridization Adsorption onto DNA Microarrays. *Anal. Chem.* **2001**, *73*, 1–7.
4. Sipova, H.; Homola, J. Surface Plasmon Resonance Sensing of Nucleic Acids: A Review. *Anal. Chim. Acta* **2013**, *773*, 9–23.
5. Lyon, L. A.; Musick, M. D.; Natan, M. J. Colloidal Au-Enhanced Surface Plasmon Resonance Immunosensing. *Anal. Chem.* **1998**, *70*, 5177–5183.
6. Kwon, M. J.; Lee, J.; Wark, A. W.; Lee, H. J. Nanoparticle-Enhanced Surface Plasmon Resonance Detection of Proteins at Attomolar Concentrations: Comparing Different Nanoparticle Shapes and Sizes. *Anal. Chem.* **2012**, *84*, 1702–1707.
7. Sendroiu, I. E.; Warner, M. E.; Corn, R. M. Fabrication of Silica-Coated Gold Nanorods Functionalized with DNA for Enhanced Surface Plasmon Resonance Imaging Biosensing Applications. *Langmuir* **2009**, *25*, 11282–11284.
8. Zhou, W. J.; Chen, Y. L.; Corn, R. M. Ultrasensitive Microarray Detection of Short RNA Sequences with Enzymatically Modified Nanoparticles and Surface Plasmon Resonance Imaging Measurements. *Anal. Chem.* **2011**, *83*, 3897–3902.
9. Bedford, E. E.; Spadavecchia, J.; Pradier, C. M.; Gu, F. X. Surface Plasmon Resonance Biosensors Incorporating Gold Nanoparticles. *Macromol. Biosci.* **2012**, *12*, 724–739.
10. Kim, E. J.; Chung, B. H.; Lee, H. J. Parts per Trillion Detection of Ni(II) Ions by Nanoparticle-Enhanced Surface Plasmon Resonance. *Anal. Chem.* **2012**, *84*, 10091–10096.
11. Hurst, S. J.; Lytton-Jean, A. K.; Mirkin, C. A. Maximizing DNA Loading on a Range of Gold Nanoparticle Sizes. *Anal. Chem.* **2006**, *78*, 8313–8318.
12. He, L.; Musick, M. D.; Nicewarner, S. R.; Salinas, F. G.; Benkovic, S. J.; Natan, M. J.; Keating, C. D. Colloidal Au-Enhanced Surface Plasmon Resonance for Ultrasensitive Detection of DNA Hybridization. *J. Am. Chem. Soc.* **2000**, *122*, 9071–9077.
13. Fang, S. P.; Lee, H. J.; Wark, A. W.; Corn, R. M. Attomole Microarray Detection of MicroRNAs by Nanoparticle-Amplified SPR Imaging Measurements of Surface Polyadenylation Reactions. *J. Am. Chem. Soc.* **2006**, *128*, 14044–14046.
14. Linman, M. J.; Abbas, A.; Cheng, Q. A. Interface Design and Multiplexed Analysis with Surface Plasmon Resonance (SPR) Spectroscopy and SPR imaging. *Analyst* **2010**, *135*, 2759–2767.
15. Jamil, M. M.; Youseffi, M.; Twigg, P. C.; Britland, S. T.; Liu, S.; See, C. W.; Zhang, J.; Somekh, M. G.; Denyer, M. C. High Resolution Imaging of Bio-molecular Binding Studies Using a Widefield Surface Plasmon Microscope. *Sens. Actuators, B* **2008**, *129*, 566–574.
16. Jamil, M. M.; Denyer, M. C.; Youseffi, M.; Britland, S. T.; Liu, S.; See, C. W.; Somekh, M. G.; Zhang, J. Imaging of the Cell Surface Interface Using Objective Coupled Widefield Surface Plasmon Microscopy. *J. Struct. Biol.* **2008**, *164*, 75–80.
17. Moh, K. J.; Yuan, X. C.; Bu, J.; Zhu, S. W.; Gao, B. Z. Surface Plasmon Resonance Imaging of Cell-Substrate Contacts with Radially Polarized Beams. *Opt. Express* **2008**, *16*, 20734–20741.
18. Peterson, A. W.; Halter, M.; Tona, A.; Bhadriraju, K.; Plant, A. L. Using Surface Plasmon Resonance Imaging To Probe Dynamic Interactions between Cells and Extracellular Matrix. *Cytometry A* **2010**, *77A*, 895–903.
19. Berguiga, L.; Roland, T.; Monier, K.; Elezgaray, J.; Argoul, F. Amplitude and Phase Images of Cellular Structures with a Scanning Surface Plasmon Microscope. *Opt. Express* **2011**, *19*, 6571–6586.
20. Wang, W.; Foley, K.; Shan, X.; Wang, S. P.; Eaton, S.; Nagaraj, V. J.; Wiktor, P.; Patel, U.; Tao, N. J. Single Cells and Intracellular Processes Studied by a Plasmonic-Based Electrochemical Impedance Microscopy. *Nat. Chem.* **2011**, *3*, 249–255.
21. Wang, W.; Wang, S. P.; Liu, Q.; Wu, J.; Tao, N. J. Mapping Single-Cell-Substrate Interactions by Surface Plasmon Resonance Microscopy. *Langmuir* **2012**, *28*, 13373–13379.
22. Wang, W.; Yang, Y. Z.; Wang, S. P.; Nagaraj, V. J.; Liu, Q.; Wu, J.; Tao, N. J. Label-Free Measuring and Mapping of Binding Kinetics of Membrane Proteins in Single Living Cells. *Nat. Chem.* **2012**, *4*, 846–853.
23. Watanabe, K.; Matsuura, K.; Kawata, F.; Nagata, K.; Ning, J.; Kano, H. Scanning and Non-scanning Surface Plasmon Microscopy to Observe Cell Adhesion Sites. *Biomed. Opt. Express* **2012**, *3*, 354–359.
24. Giebel, K. F.; Bechinger, C.; Herminghaus, S.; Riedel, M.; Leiderer, P.; Weiland, U.; Bastmeyer, M. Imaging of Cell/Substrate Contacts of Living Cells with Surface Plasmon Resonance Microscopy. *Biophys. J.* **1999**, *76*, 509–516.
25. Wang, S. P.; Shan, X. N.; Patel, U.; Huang, X. P.; Lu, J.; Li, J. H.; Tao, N. J. Label-Free Imaging, Detection, and Mass Measurement of Single Viruses by Surface Plasmon Resonance. *Proc. Natl. Acad. Sci. U.S.A.* **2010**, *107*, 16028–16032.
26. Weichert, F.; Gaspar, M.; Timm, C.; Zybin, A.; Gurevich, E.; Engel, M.; Muller, H.; Marwedel, P. Signal Analysis and Classification for Surface Plasmon Assisted Microscopy of Nanoobjects. *Sens. Actuators, B* **2010**, *151*, 281–290.
27. Zybin, A.; Kuritsyn, Y. A.; Gurevich, E. L.; Temchura, V. V.; Uberla, K.; Niemax, K. Real-Time Detection of Single

Immobilized Nanoparticles by Surface Plasmon Resonance Imaging. *Plasmonics* **2010**, *5*, 31–35.
28. Gurevich, E. L.; Temchura, V. V.; Uberla, K.; Zybin, A. Analytical Features of Particle Counting Sensor Based on Plasmon Assisted Microscopy of Nano Objects. *Sens. Actuators, B* **2011**, *160*, 1210–1215.
29. Shan, X. N.; Diez-Perez, I.; Wang, L. J.; Wiktor, P.; Gu, Y.; Zhang, L. H.; Wang, W.; Lu, J.; Wang, S. P.; Gong, Q. H.; *et al.* Imaging the Electrocatalytic Activity of Single Nanoparticles. *Nat. Nanotechnol.* **2012**, *7*, 668–672.
30. Berger, C. E.; Kooyman, R. P.; Greve, J. Resolution in Surface Plasmon Microscopy. *Rev. Sci. Instrum.* **1994**, *65*, 2829–2836.
31. Kano, H.; Mizuguchi, S.; Kawata, S. Excitation of Surface Plasmon Polaritons by a Focused Laser Beam. *J. Opt. Soc. Am. B* **1998**, *15*, 1381–1386.
32. Kano, H.; Knoll, W. A Scanning Microscope Employing Localized Surface-Plasmon-Polaritons as a Sensing Probe. *Opt. Commun.* **2000**, *182*, 11–15.
33. Tanaka, T.; Yamamoto, S. Laser-Scanning Surface Plasmon Polariton Resonance Microscopy with Multiple Photodetectors. *Appl. Opt.* **2003**, *42*, 4002–4007.
34. Somekh, M. G.; Liu, S. G.; Velinov, T. S.; See, C. W. High-Resolution Scanning Surface-Plasmon Microscopy. *Appl. Opt.* **2000**, *39*, 6279–6287.
35. Somekh, M. G.; Liu, S. G.; Velinov, T. S.; See, C. W. Optical V(z) for High-Resolution 2π Surface Plasmon Microscopy. *Opt. Lett.* **2000**, *25*, 823–825.
36. Huang, B.; Yu, F.; Zare, R. N. Surface Plasmon Resonance Imaging Using a High Numerical Aperture Microscope Objective. *Anal. Chem.* **2007**, *79*, 2979–2983.
37. Johansen, K.; Arwin, H.; Lundstrom, I.; Liedberg, B. Imaging Surface Plasmon Resonance Sensor Based on Multiple Wavelengths: Sensitivity Considerations. *Rev. Sci. Instrum.* **2000**, *71*, 3530–3538.
38. Otte, M. A.; Sepulveda, B.; Ni, W. H.; Juste, J. P.; Liz-Marzan, L. M.; Lechuga, L. M. Identification of the Optimal Spectral Region for Plasmonic and Nanoplasmonic Sensing. *ACS Nano* **2010**, *4*, 349–357.
39. Nelson, B. P.; Frutos, A. G.; Brockman, J. M.; Corn, R. M. Near-Infrared Surface Plasmon Resonance Measurements of Ultrathin Films. 1. Angle Shift and SPR Imaging Experiments. *Anal. Chem.* **1999**, *71*, 3928–3934.
40. Lozovski, V. Visualization of Nano-Sized Objects by Scattering of Surface Plasmon Polariton Theoretical Aspects of the Problem. *J. Comput. Theor. Nanosci.* **2012**, *9*, 859–863.
41. Chen, Y. L.; Nguyen, A.; Niu, L. F.; Corn, R. M. Fabrication of DNA Microarrays with Poly(L-glutamic acid) Monolayers on Gold Substrates for SPR Imaging Measurements. *Langmuir* **2009**, *25*, 5054–5060.
42. Steel, A. B.; Herne, T. M.; Tarlov, M. J. Electrochemical Quantitation of DNA Immobilized on Gold. *Anal. Chem.* **1998**, *70*, 4670–4677.
43. Jain, A.; Liu, R. J.; Ramani, B.; Arauz, E.; Ishitsuka, Y.; Ragunathan, K.; Park, J.; Chen, J.; Xiang, Y. K.; Ha, T. Probing Cellular Protein Complexes Using Single-Molecule Pull-Down. *Nature* **2011**, *473*, 484–488.
44. Adessi, C.; Matton, G.; Ayala, G.; Turcatti, G.; Mermod, J. J.; Mayer, P.; Kawashima, E. Solid Phase DNA Amplification: Characterisation of Primer Attachment and Amplification Mechanisms. *Nucleic Acids Res.* **2000**, *28*, e87.